PCCP

PAPER

View Article Online
View Journal | View Issue

Cite this: *Phys. Chem. Chem. Phys.*, 2016, **18**, 21780

Understanding the fundamental electrical and photoelectrochemical behavior of a hematite photoanode†

Mario R. S. Soares,[a] Ricardo H. Gonçalves,[a] Içamira C. Nogueira,[b] Jefferson Bettini,[c] Adenilson J. Chiquito[d] and Edson R. Leite*[a]

Received 27th May 2016,
Accepted 12th July 2016

DOI: 10.1039/c6cp03680e

www.rsc.org/pccp

Hematite is considered to be the most promising material used as a photoanode for water splitting and here we utilized a sintered hematite photoanode to address the fundamental electrical, electrochemical and photoelectrochemical behavior of this semiconductor oxide. The results presented here allowed us to conclude that the addition of Sn^{4+} decreases the grain boundary resistance of the hematite polycrystalline electrode. Heat treatment in a nitrogen (N_2) atmosphere also contributes to a decrease of the grain boundary resistance, supporting the evidence that the presence of oxygen is fundamental for the formation of a voltage barrier at the hematite grain boundary. The N_2 atmosphere affected both doped and undoped sintered electrodes. We also observed that the heat treatment atmosphere modifies the surface states of the solid–liquid interface, changing the charge-transfer resistance. A two-step treatment, with the second being performed at a low temperature in an oxygen (O_2) atmosphere, resulted in a better solid–liquid interface.

Introduction

The conversion of solar energy into fuels, such as hydrogen (H_2), is a promising method to store solar energy;[1] moreover, using a photoelectrochemical cell (PEC) is an elegant and feasible method to convert it.[1,2] Hematite (α-Fe_2O_3), an n-type semiconductor with high photoelectrochemical stability, is considered the most promising material to be used as a photoanode for water splitting (with a potential to convert 16.8% of the sun's energy into hydrogen).[2] However, its use presents many challenges, such as: (i) a large requisite overpotential for water oxidation; (ii) a relatively low absorption coefficient, requiring thick films for efficient light absorption; (iii) a poor majority carrier (electrons) conductivity; and (iv) a short minority carrier diffusion length (holes).[1,3] These intrinsic properties of the hematite hinder the PEC's performance by increasing the electron/hole recombination. In general, there are three main electron/hole recombination pathways that can occur in bulk and in solid–solid and solid–liquid (electrolyte) interfaces.[2,3] The bulk electron/hole recombination process is directly related to the poor electronic conductivity and short hole collection depth of the hematite. Besides, the recombination can also occur in two different solid–solid interfaces: in the hematite/transparent conducting oxide (TCO) electrode[4] and in the hematite/hematite grain boundary.[5] Finally, there are significant recombination processes in the solid–liquid (electrolyte) interfaces; recombination losses due to the back-injection of electrons, from the TCO exposed area, into the electrolyte;[6] and a recombination that occurs in the hematite–electrolyte interface, as a result of surface states and traps that delay the hole transfer from the valence band of the semiconductor to the electrolyte.[7–10] It is clear that the junction of these several electron/hole recombination pathways leads to a hematite photoanode with a low photocurrent and large overpotential for water oxidation.

In recent years, an impressive amount of research has been done to understand and reduce the recombination processes that occur in each pathway. For instance, to reduce bulk recombination researchers mainly focused on producing nanostructured hematite with different morphologies and/or doping the ionic semiconductor with different metals.[1,2] These strategies decrease bulk recombination by shortening the hole transport

[a] *Chemistry Department, Federal University of São Carlos, São Carlos, SP, Brazil. E-mail: edson.leite@pq.cnpq.br*
[b] *Postgraduate Program in Materials Engineering, Federal Institute of Maranhão – IFMA, São Luís, MA, Brazil*
[c] *Laboratório Nacional de Nanotecnologia LNNano, Caixa Postal 6192, BR-13083970, Campinas, SP, Brazil*
[d] *Physics Department, Federal University of São Carlos, São Carlos, SP, Brazil*

† Electronic supplementary information (ESI) available: Optimization of the sintering process and structural Rietveld refinement details. Schematic representation of the boundary space charge and the concentration of associated charged defects in the undoped hematite, schematic representation of the brick-layer model used for SSIS analysis, SSIS analysis of the samples doped with 2.0 wt% of SnO_2 and treated at different atmospheres and analysis of the *J vs. E* plot. See DOI: 10.1039/c6cp03680e

distance and by increasing its electrical conductivity, respectively. Hematite has been modified with various dopants (transition metals and non-transition metals) and there are several good reviews in the literature that describe the effect of these dopants on the electronic behaviour of the hematite.[2,3,11] Among the non-transition metal dopants, Sn has been widely used to modify the electronic conductivity of the hematite[11] and more recently, Sn doping has also been used to modify the surface defect states of hematite, resulting in a shift of the onset of the water oxidation reaction in the positive direction.[12,13]

It is clear that a variety of electron/hole combination pathways and interfaces are related to the thin film morphology of the hematite photoanode, and this morphology is a result of its manufacturing technique. In contrast to semiconductor technology, where there is an extensive use of single crystalline materials and/or epitaxial films grow over single crystalline substrates, hematite photoanode manufacturing techniques are based on polycrystalline (with grain sizes on the nanometer scale) and mesoporous films, normally textured along the [110] direction and grown over a TCO substrate.[14] Thus, this material is characterized by: (i) non-uniform grain sizes; (ii) a columnar structure; (iii) porosity; (iv) impurity segregation; and (v) grain–grain misorientation, forming homo-junctions and hetero-junctions. Fig. 1a illustrates, in a simplified way, microstructural features and interfaces found in a typical nanostructured hematite photoanode.

The morphological complexity of the hematite photoanode makes it harder to identify the dominant loss process and to assess how these processes impact the final photoanode performance. Few are the works reported in the literature that studied the solid–solid interface and the importance of this electron/hole recombination pathway in the overall hematite photoanode performance.[5,14,15] The solid–solid interface, in particular the grain boundary, should have an important impact on the electronic properties of this electrode. In electronic ceramics based on transition metal oxide semiconductors, it is well established that the grain boundary controls the electronic properties, increasing the resistance and generating non-ohmic behavior.[16] An obvious question that arises from this analysis is: does the grain boundary control the electrical properties of a hematite?

Here we intend to address and answer the above question. Therefore, we used the simplest hematite photoanode, *i.e.*, a sintered polycrystalline hematite electrode. As illustrated in Fig. 1b, the sintered photoanode shows a smaller number of interfaces and maintains important microstructural features, such as grain boundaries and a surface–electrolyte interface. In this kind of photoanode the recombination at the hematite/transparent conducting oxide (TCO) electrode and the recombination losses resulting from the back-injection of electrons from exposed areas of the TCO into the electrolyte are not present. Besides, the use of a metallic electrode with a suitable work function must provide an ohmic contact between the sintered hematite and the metallic electrode, minimizing the loss at its interface. Here we will show how the addition of Sn^{4+} (as a dopant) and the heat treatment atmosphere modify the electrical properties of the sintered ceramic pellet as well as impact the electrochemical and photoelectrochemical properties of the ceramic electrode.

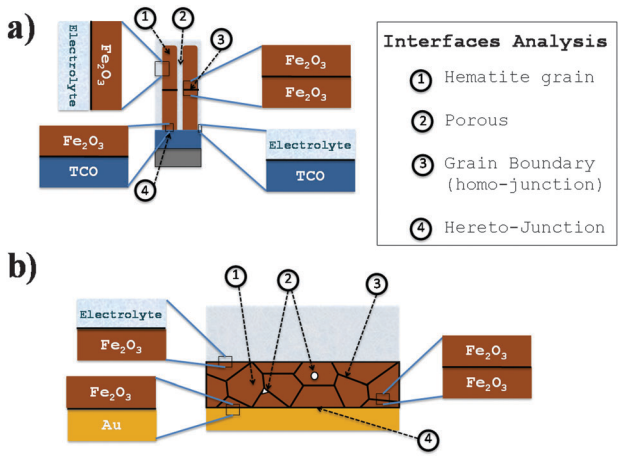

Fig. 1 Illustration of porous and dense (sintered) hematite thin films: (a) a typical hematite photoanode processed by different thin film deposition processes; (b) a polycrystalline ceramic hematite photoanode.

Experimental

Sample preparation

High purity hematite (α-Fe_2O_3) and SnO_2 powder were used as raw materials to prepare the polycrystalline ceramic pellet. In this work we prepared pure hematite as well as hematite doped with 0.1, 1.0 and 2.0 wt% of SnO_2. The oxides were homogenized by mechanically mixing with isopropyl alcohol in an ultrasonic point for 10 min. After drying, the powders were granulated and pressed (55 MPa) into pellets with a diameter of 13 mm and a thickness of $\sim$2 mm. In our experiment, besides the incorporation of Sn in the hematite lattice, we need a sintered sample with high density (minimum of porosity). In order to obtain the minimum of porosity we need high temperature to promote the pore elimination and densification process. A set of experiments were performed in order to optimize the sintering temperature. In this optimization we aimed at a final sintered relative density of around 99% and a final grain size of similar dimensions, independent of the SnO_2 doping level (for details see ESI,† Fig. S1). All the samples were sintered in a box-type furnace for 6 h at 1300 °C (the best temperature to obtain the minimum of porosity) and all sintering procedures were carried out in atmospheric air. In order to evaluate the effect of the atmosphere on the electrical and electrochemical properties, samples sintered in air were further heat-treated in a tube furnace, at 850 °C for 20 min with an N_2 and/or O_2 flow.

Structural and microstructural characterization

Apparent densities after sintering were determined by Archimed's method and crystalline phases were analyzed by X-ray diffraction using CuKα radiation. Based on the X-ray data, the Rietveld method was applied to adjust the cell and determine lattice parameters and the unit cell volume of sintered samples with

different SnO_2 content. The Rietveld refinement of the measured XRD was carried out using the general structure analysis (GSAS) program.[17] The background was corrected using a Chebyschev polynomial of the first kind and the diffraction peak profiles were better adjusted using the Thompson–Cox–Hastings pseudo-Voigt (pV-TCH) function.[18] A field emission scanning electron microscope (FE-SEM) was used to perform the microstructural characterization of the polished and thermally etched samples. Dopant segregation at the grain boundary, for the sintered hematite sample doped with 2.0 wt% of SnO_2, was investigated using high resolution transmission electron microscopy (HRTEM) and scanning transmission electron microscopy (STEM) integrated with energy dispersive spectroscopy analysis (EDS). The analysis was performed at 200 kV with a spatial resolution better than 0.5 nm. The HRTEM-STEM/EDS sample was prepared by *in situ* milling employing focus ion milling equipment.

Electrical, electrochemical and photoelectrochemical characterization

For electrical, electrochemical and photoelectrochemical characterization, the samples were polished with #1200 mesh sandpaper and gold electrodes (ohmic contact) were deposited by electron beam evaporation. The current density *versus* electric field (J *vs.* E) for all samples was measured at room temperature (two points method) using a d.c. voltage source. The samples were also characterized by solid state impedance spectroscopy (SSIS) using an impedance analysis in the frequency range of 40 Hz to 110 MHz, without bias and with an amplitude potential of 1 V.

The electrochemical and photoelectrochemical measurements were performed on sintered hematite pellets with ~11 mm diameter and 1 mm thickness. A gold wire was attached to the ohmic contact using a silver epoxy adhesive while the electrical insulation from back and sides of the sample were achieved by applying an epoxy coating. The electrochemical and photoelectrochemical measurements were carried out in a standard three-electrode cell using the sintered hematite as the working electrode, Ag/AgCl in a KCl saturated solution as the reference electrode and a platinum wire as the counter electrode. A 1.0 M NaOH (pH = 13.6) solution was used as the electrolyte. A scanning potentiostat was used to measure the dark and illuminated currents at a scan rate of 20 mV s^{-1}. Sunlight (1000 W m^{-2}) was simulated using a 450 W xenon lamp (Osram, ozone free) and an AM1.5 filter. Light intensity was set at 100 mW cm^{-2}. The Mott–Schottky analysis and the electrochemical impedance spectroscopy (EIS) measurements were performed using a potentiostat/galvanostat with a three-electrode configuration in 1.0 M of NaOH solution. Frequencies ranging from 10 mHz to 100 kHz, with a 10 mV of amplitude potential and a bias voltage of 0.55 to 1.75 V *vs.* RHE were applied. The EIS was carried out with and without light.

Results and discussion

Microstructural characterization

Table 1 summarizes the microstructural and structural characterization of the sintered hematite samples doped with different SnO_2 concentrations. Values of relative density above 98% are observed, regardless of the doping level. The microstructural evolution of the sintered samples was followed by FE-SEM analysis. Fig. 2 displays the backscattered FE-SEM images of pure (Fig. 2a) and SnO_2-doped hematite (Fig. 2b–d). The contrast in these pictures is attributed to the superficial electron channeling, which is related to the crystallographic orientation of the grains. All samples show high-density microstructures with trapped pores, pores located at the grain boundary and elongated grains. Besides, as the doping level increases, we observe a decrease in the mean grain size and a narrowing in the grain size distribution (see insets in Fig. 2a–d and Table 1). The decrease in mean grain size with the increase of the doping level is indirect evidence of the Sn cation segregating at the grain boundary during the sintering process.[19] Actually, it is important to point out that the dopant segregation in the hematite has been reported by different authors,[20,21] corroborating with our indirect evidence.

Table 1 Microstructural and structural data of the sintered hematite sample

Sample	Relative density (%)	Mean grain size (μm)	Lattice parameter a (Å)	Lattice parameter c (Å)	Cell volume (Å^3)
Undoped	98.9	50.9	5.033	13.744	301.60
0.1 wt% SnO_2	98.5	53.9	5.034	13.747	301.70
1.0 wt% SnO_2	98.4	46.4	5.037	13.751	302.11
2.0 wt% SnO_2	98.4	34.2	5.038	13.754	302.33

To gain a better understanding of the Sn ion distribution at the grain boundary area, the sintered hematite sample doped with 2.0 wt% of SnO_2 was characterized by HRTEM-STEM/EDS analysis. Fig. 3a and b depicts the typical HRTEM images of the grain boundary region, showing grain boundaries with intergranular films (with thickness ranging from 0.9 nm to 2 nm)

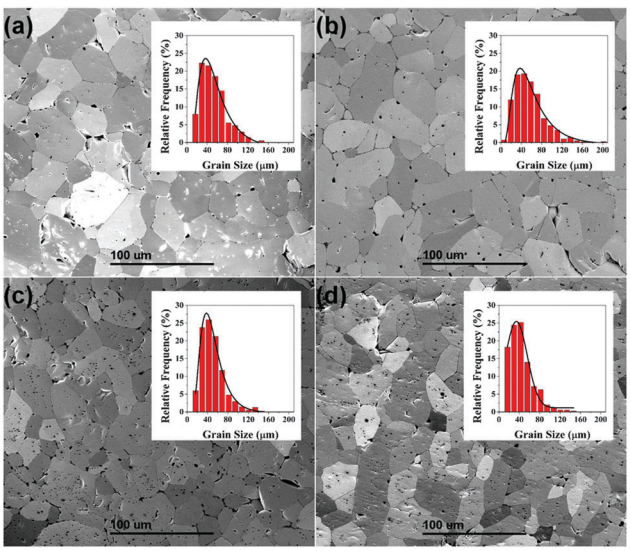

Fig. 2 Backscattered FE-SEM images of pure (a) and SnO_2-doped hematite; (b) 0.1 wt% of SnO_2; (c) 1.0 wt% SnO_2; and (d) 2.0 wt% SnO_2. The inset shows the grain size distribution of each sample.

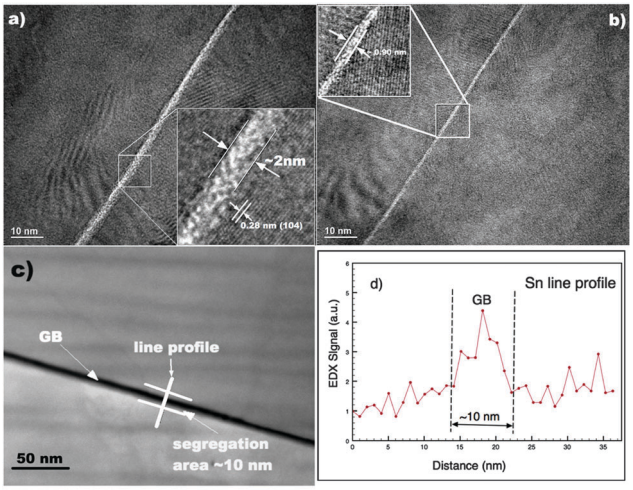

Fig. 3 (a) HRTEM-STEM/EDS analysis of the sintered hematite sample doped with 2.0 wt% of SnO_2; (b) HRTEM images of two different grain boundary regions. The insets show details of the intergranular films; (c) the BF-STEM image, indicating the region analyzed by the EDS line profile; (d) EDS line profile analysis.

formed by several atomic layers (see insets in Fig. 3a and b). The bright field (BF) STEM image and X-ray line profile analysis (EDS line profile analysis) for the same sample is shown in Fig. 3c and d, respectively. The EDS line profile, performed in the region pointed out in Fig. 3c, indicates the presence of an Sn-rich segregation area of ~10 nm (Fig. 3d). This analysis confirms that the intergranular film is rich in Sn and that there is the formation of a segregation region near the grain boundary, indicating a heterogeneous distribution of Sn ions in the sintered hematite ceramics.

In this work, the Rietveld method was applied to analyze the lattice parameters and unit cell volume of doped and undoped sintered hematite (Fig. S2 in the ESI† illustrates the structural refinement of these samples) and the results are shown in Table 1. The measured diffraction pattern was well adjusted to the Inorganic Crystal Structure Database (ICSD) card no. 15840[22] confirming that the hematite crystals have a trigonal structure with the Hermann–Mauguin symmetry space group $R\bar{3}c$ and six molecular formula units per cell (Z = 6). Only α-Fe_2O_3 was identified as a crystalline phase, even for the highest doping level. For the doped material, cell volume showed a small positive deviation from the undoped hematite, suggesting the incorporation of the Sn cation (assuming Sn^{4+}) in the lattice structure of α-Fe_2O_3. Besides, this small deviation should be related to the segregation of the dopant at the grain boundary region. The substitution of Fe^{3+} by Sn^{4+} in the α-Fe_2O_3 structure as well as its segregation will generate a charge compensation that can be either ionic or electronic. The consequence of these phenomena will be discussed below.

Electrical characterization

In order to understand the electrical behavior of an ionic oxide semiconductor, such as hematite, it is necessary to analyze its defect chemistry. In α-Fe_2O_3, the intrinsic ionic disorder is associated with the formation of Schottky defects,[23,24] which can be described by the quasi-chemical reaction as:

$$\text{null} \rightarrow 2V_{Fe}''' + 3V_O^{\bullet\bullet} \quad (1)$$

where V_{Fe}''' is the charged iron vacancy and $V_O^{\bullet\bullet}$ is the charged oxygen vacancy (here we are using the Kroger–Vink notation).

An important characteristic of the Schottky defect is that it requires a region of lattice discontinuity, such as a grain boundary, and a dislocation or a free surface to occur. This discontinuity is referred to as a sink for defects. An important effect resulting from the equilibrium of ionic defects with a discontinuity (such as a grain boundary) is the formation of a surface electrical potential, associated with an excess of surface ionic charge. The energy for the Schottky disorder formation can be separated into individual cation (gV_{Fe}) and anion (gV_O) formation energies. Differences in the cation and anion energy formation lead to different surface ion concentrations from those in the bulk. Thus, the discontinuity becomes nonstoichiometric and bears a net charge. In order to achieve the overall electrical neutrality, an adjacent space-charged layer compensates the surface charge. At equilibrium, there is an electrostatic potential difference between the surface and the interior.[25]

Considering an undoped α-Fe_2O_3, the equilibrium of cations and anions with the discontinuity (surface or grain boundary) can be written as:

$$2Fe_{Fe}^{\times} + 3O_O^{\times} \leftrightarrows 2Fe_{Sup}^{\bullet\bullet\bullet} + 3O_{Sup}'' + 2V_{Fe}''' + 3V_O^{\bullet\bullet} \quad (2)$$

$$Fe_{Fe}^{\times} = Fe_{Sup}^{\bullet\bullet\bullet} + V_{Fe}''' \quad (3)$$

$$O_O^{\times} = O_{Sup}'' + V_O^{\bullet\bullet} \quad (4)$$

where the subscript term Sup indicates a defect located in the discontinuity. From eqn (2) we can write the following charge neutrality condition:

$$n + 3[V_{Fe}'''] = p + 2[V_O^{\bullet\bullet}] \quad (5)$$

where n and p is the electron and hole concentration, respectively, $[V_{Fe}''']$ is the charged iron vacancy concentration and $[V_O^{\bullet\bullet}]$ the charged oxygen vacancy concentration.

Theoretical studies of point defects in hematite[26,27] suggest the following values for the defect energy formation: gV_{Fe} raging from 55.0 to 55.2 eV and gV_O raging from 20.3 to 23.8 eV. These studies indicate an important characteristic for the Schottky defect in hematite, *i.e.*, the energy required to form $V_O^{\bullet\bullet}$ is smaller than the energy to form V_{Fe}'''.

The electrostatic potential $\phi(x)$ (that depends on the position x) can be estimated by the Kliewer and Koehler formalism.[28] At any point of the crystal, the ion vacancy concentration is controlled by (i) the vacancy energy formation, (ii) the effective charge (z) and (iii) the electrostatic potential $\phi(x)$. For hematite, these concentrations can be expressed as:

$$[V_{Fe}'''](x) = 2\exp[-(gV_{Fe} - 3e\phi(x))/kT] \quad (6)$$

$$[V_O^{\bullet\bullet}](x) = 3\exp[-(gV_O + 2e\phi(x))/kT] \quad (7)$$

where k is the Boltzmann constant and T the absolute temperature.

Far away from the discontinuity (a grain boundary, for instance), at $x = \infty$, $\phi(x) = \phi_\infty$. The overall electric neutrality requires that:

$$3\left[V'''_{Fe}\right]_\infty = 2\left[V^{\bullet\bullet}_{O}\right]_\infty \quad (8)$$

Considering eqn (6)–(8), we can obtain the electrostatic potential ϕ_∞ at the interior of the crystal:

$$\phi_\infty = 1/5(gV_{Fe} - gV_O) \quad (9)$$

Based on eqn (9), we notice that the magnitude and the sign of the space charge potential in an undoped hematite are determined by the difference in the cation and anion vacancy formation energies. By convenience, we assume that $\phi(x) = 0$ for $x = 0$, *i.e.*, the potential is zero at the grain boundary. Taking into account eqn (2)–(4) and since $gV_{Fe} > gV_O$, we can determine that the space charge potential near the grain boundary will be positive, rich in $V^{\bullet\bullet}_O$ and depressed of V'''_{Fe}, and consequently a boundary with anion $\left(O''_{Sup}\right)$ excess will be formed. An estimate for ϕ_∞, considering the theoretical values for gV_{Fe} and gV_O, gives $\phi_\infty \cong +6$ V. Fig. S3 (see ESI†) describes in a schematic way the boundary space charge and the concentration of associated charged defects in the undoped hematite.

Now, we need to understand how this defect analysis can help us understand the electrical behavior of the hematite. Fig. 4 shows the *J vs. E* plot for the sintered sample as well as for samples that were heat-treated at 850 °C for 20 min with an O_2 and/or N_2 flow. We noticed a very high electric resistivity and ohmic behavior, regardless of the treatment applied to the samples. However, it is clear that the heat treatment in different atmospheres modifies the resistivity of the sample. For instance, the sample treated with an O_2 flow shows a resistivity of 3.5×10^8 Ω cm, while samples that were sintered or treated with an N_2 flow show a resistivity of 2.3×10^8 Ω cm and 2.8×10^8 Ω cm, respectively. These results suggest that the presence of O_2 increases the resistivity. Since the heat treatment was performed at a temperature smaller than the sintering temperature, the modification in the resistivity cannot be associated with a modification in the overall defect concentration. However, the temperature used must be enough to promote the diffusion of oxygen through the grain boundary, creating a new equilibrium condition in the defect concentration near the discontinuity. This interpretation is consistent with the defect chemistry analysis presented before, and is supported by previous works that attribute the high resistivity of sintered hematite to oxygen adsorption during the cooling process.[29,30]

The electrical characterization of the undoped hematite shows a very high resistivity, which makes any practical application of this semiconductor material as a photoanode impractical. One way to decrease its resistivity is introducing donor doping elements, such as cations with a higher valence than Fe^{3+}. In the present work, we selected Sn^{4+}. Fig. 5a shows the *J vs. E* plot for the sintered hematite, with several SnO_2 concentrations. It is clear that even a small concentration of

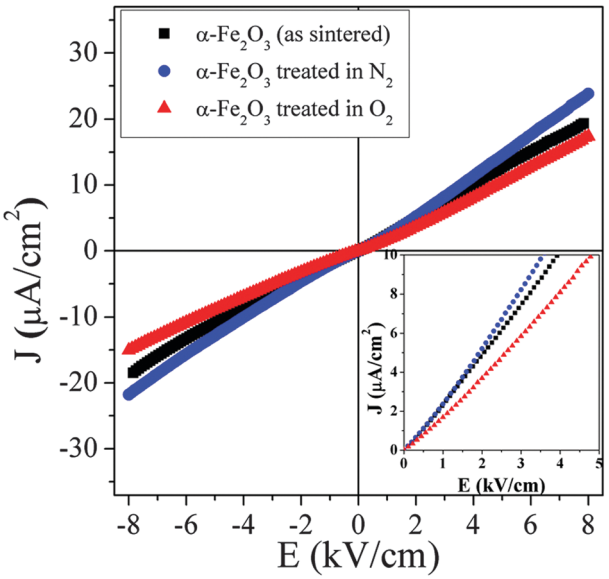

Fig. 4 *J vs. E* plot for the sintered undoped hematite (black squares) and heat-treated samples at 850 °C for 20 min with oxygen (red triangle) and nitrogen flow (blue circles). The inset shows a zoom of the *J vs. E* plot, where a clear influence of the atmosphere on the undoped hematite can be seen.

dopant promotes a decrease in resistivity. For example, the undoped material shows a resistivity of 2.3×10^8 Ω cm, while the sintered hematite doped with 2.0 wt% of SnO_2 shows a resistivity of 1.1×10^3 Ω cm, *i.e.*, a reduction of 5 orders of magnitude. We also noticed that the doped material shows a non-ohmic behavior. This non-ohmic behavior is quite evident in Fig. 5b, where we show the *J vs. E* plot for the sintered hematite doped with 2.0 wt% of SnO_2, as well as for the doped samples heat-treated at 850 °C with O_2 or N_2 flow. The non-ohmic behavior observed in the doped material must be associated with the heterogeneous distribution of the dopant, resulting in an electrical property controlled by the grain boundary.[16] Fig. 5b also shows that the heat treatment with a N_2 flow decreases resistivity while the heat-treatment with an O_2 flow increases resistivity. Actually, this is strong evidence that nitrogen and oxygen modify grain boundary resistance, as proposed before.

The previous results strongly suggest that for undoped and doped hematite the electrical behavior is controlled by the grain boundary. A good way to verify this hypothesis is to use the SSIS. The SSIS is a classic tool used to characterize grain boundary effects in polycrystalline semiconductors; assuming a brick-layer model (see Fig. S4 in the ESI†), the presence of a voltage barrier at the grain boundary is associated with a parallel RC equivalent electrical circuit, or a semi-circle at an intermediate frequency in the Nyquist plot.[31,32] This behavior is typical of a grain boundary effect and is normally associated with a back-to-back Schottky barrier formation. Fig. 5c shows a SSIS analysis of sintered undoped and doped samples with different SnO_2 concentrations. These measurements were performed at room temperature and it is clear that the total resistance of the sample decreased as the SnO_2 concentration increased. The Nyquist plots, for the samples doped with 1.0 and 2.0 wt%, show a depressed semicircle

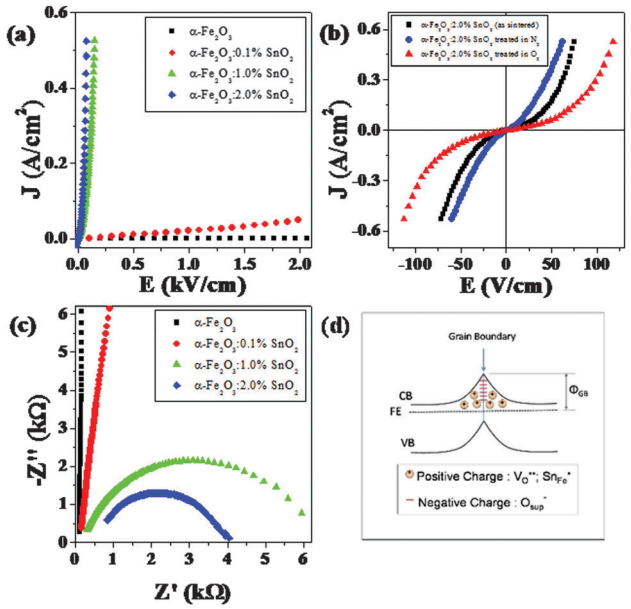

Fig. 5 Electronic behavior of SnO_2 doped hematite sintered samples: (a) the *J vs. E* plot for the sintered sample doped with different SnO_2 concentrations; (b) the *J vs. E* plot for the doped samples with 2.0 wt% of SnO_2 and heat-treated at 850 °C with oxygen and nitrogen flows; (c) SSIS analysis (Nyquist plot) of sintered undoped and doped samples, with different SnO_2 concentrations; and (d) the defect and energy band model of a Schottky barrier at the grain boundary of the hematite.

displaced from the origin (in the Z' axis). The displacement can be associated with bulk resistance (grain resistance) while the non-perfect semicircle can be associated with the capacitive and resistive nature of the grain boundary.

It is interesting to observe that by increasing the doping level we observe an increase of the bulk's resistance and a decrease of the grain boundary's resistivity. This behavior must be related to the Sn segregation, indicating that the presence of the Sn ions in the grain boundary region modifies its electrical resistance. Actually, the segregation of Sn ions decreases grain boundary resistance. We would like to point out that the deviation of the ideal semicircle reported here in the SSIS analysis can be associated with an inhomogeneous microstructure that differs from the brick-layer model (even if a single grain boundary relaxation time is involved)[31,32] and not with grain boundaries with different relaxation times. We performed a SSIS analysis also in the samples doped with 2.0 wt% of SnO_2 and treated at different atmosphere flows (see Fig. S5 in the ESI†) and the results clearly show that the atmosphere has a direct impact on the grain boundary resistance.

The SSIS and the *J vs. E* analysis show that the introduction of Sn ions modifies hematite conductivity, consequently modifying the grain boundary's resistivity. This observation allowed us to assume that the electrical behavior of the hematite is controlled by the grain boundary's resistivity. Thus, we can use the non-linear nature of the *J vs. E* curve to estimate the grain boundary's drop of voltage. As illustrated in Fig. S6 (see ESI†), we can define two important parameters in the *J vs. E* plot with non-ohmic behavior, (i) the slope at the low electric field that is inversely proportional to the grain boundary resistance in a polycrystalline semiconductor material and (ii) the breakdown voltage (V_{Br}) at a high electrical field. Focusing on the breakdown voltage, we can observe that the V_{Br} for the sample that was doped (2.0 wt%) and treated in N_2 shows the smallest value ($V_{Br} \sim 8$ V cm^{-1}), and the sample treated in O_2 shows the biggest value ($V_{Br} \sim 35$ V cm^{-1}) (see Fig. S7, ESI†). Considering that the sintered hematite pellet can be described by a brick-layer model (see Fig. S4 in the ESI†), we can write that V_{Br} is given by:

$$V_{Br} = V_{GB} \cdot n \quad (10)$$

where V_{GB} is the voltage drop given the grain boundary and n is the number of grain boundaries in series. For a given sample with grain size G and width L, we can write $n = L/G$. Thus we can write that V_{GB} is given by:

$$V_{GB} = V_{Br}(G/L) \quad (11)$$

Considering eqn (11) we estimated the values of V_{GB} for the samples doped with 2.0 wt% of SnO_2 and treated in different atmospheres. The values obtained are 30 mV, 70 mV and 140 mV for each grain boundary, for the samples treated in N_2 and for the ones that were sintered and treated in O_2, respectively.

The introduction of Sn ions modifies the defect chemistry equilibrium at the grain boundary region and here we postulate two hypotheses to explain the effect of Sn^{4+} (assuming valence 4+ for the Sn ion) on the electrical behavior of the hematite.

Hypothesis one. Considering the heterogeneous incorporation of Sn^{4+} while substituting Fe^{3+} in the hematite lattice, we can write for ionic compensation:

$$3SnO_2 \xrightarrow{\alpha\text{-}Fe_2O_3} 3Sn_{Fe}^{\bullet} + 6O_O^{\times} + V_{Fe}^{'''} \quad (12)$$

Considering electronic compensation, the following equation can be written:

$$SnO_2 \xrightarrow{\alpha\text{-}Fe_2O_3} Sn_{Fe}^{\bullet} + 2O_O^{\times} + e' \quad (13)$$

The electronic compensation brings the possibility of Fe^{3+} reduction to Fe^{2+}, according the eqn (14)

$$Fe_{Fe}^{\bullet\bullet\bullet} + e' \rightarrow Fe_{Fe}' \quad (14)$$

where Fe_{Fe}' is Fe^{2+}. Based on eqn (12) and (13), Sn^{4+} introduces electrons near Fe^{3+} sites and considering eqn (14), the reduction to Fe^{2+} must occur. Considering the electronic conduction of hematite is a result of polaron hopping,[33,34] the formation of Fe^{2+} sites can improve the electrical conductivity, especially near the grain boundary.

The formation of Fe^{2+} near the grain boundary is consistent with the reduction of the grain boundary resistance. Besides, it also explains the dependency of the grain boundary's resistivity of the doped material on the atmosphere during the heat treatment. In the oxygen flow, the oxidation of Fe^{2+} to Fe^{3+} must occur, resulting in a negatively charged specie at the grain surface $\left(O_{Sup}''\right)$ and a decrease of Fe^{2+} concentration in the grain boundary region. Consequently, an increase in the grain

boundary's resistivity must take place (see Fig. S5 in the ESI† that shows the increase of grain boundary resistance in oxygen flow).

Hypothesis two. Besides the formation of Fe^{2+}, another explanation for the decrease in grain boundary resistance is the incorporation of Sn^{4+} ($Sn_{Fe}^{\bullet}$) that leads to a decrease of $[V_O^{\bullet\bullet}]$ near the grain boundary with subsequent decreases in the concentration of negative charges at the interface (mainly O''_{Sup}). Under this condition we can write $n = [Sn_{Fe}^{\bullet}]$. In this case, the high resistivity of the grain boundary is related to the formation of back-to-back Schottky barriers, in which the depletion layer (W) is formed by a positive charge, such as $V_O^{\bullet\bullet}$ and $Sn_{Fe}^{\bullet}$ with a donor density N_d. A negative charge is formed during the sintering process and is basically composed of O''_{Sup}, with surface state density of N_S. The electric neutrality condition for the material is given by $N_S = 2N_dW$. In the back-to-back Schottky barriers, a potential barrier Φ_{GB} is formed at the grain boundary. Considering this model, Φ_{GB} is proportional to N_S^2 and inversely proportional to N_d ($\Phi_{GB} \propto N_S^2/N_d$). It is obvious that a decrease in $[O''_{Sup}]$ promotes a decrease in N_S and consequently a decrease of Φ_{GB}, resulting in a less resistive grain boundary. This hypothesis also explains the dependency of the grain boundary resistivity of the doped material on the atmosphere during the heat treatment. Fig. 5d illustrates a defect and energy band model that describes a Schottky barrier at the hematite's grain boundary.

Electrochemical and photoelectrochemical characterization

In the previous discussion we described the impact of Sn^{4+} doping and the heat treatment atmosphere on the grain boundary's (solid–solid interface) resistance. The doped sample showed a low resistivity that allows us to perform good electrochemical characterization of the sintered hematite. The main focus of this characterization is to verify the impact of the heat treatment atmosphere on the electrochemical and photoelectrochemical properties of the sintered hematite electrode, *i.e.*, in the solid–liquid interface. These characterizations were performed in three samples (all doped hematite with 2.0% of SnO_2): a sample doped and heat-treated in O_2 (850 °C); a sample doped and heat-treated in N_2 (850 °C); and a sample doped and heat-treated in N_2 at 850 °C and then re-treated in O_2 at 350 °C. The main idea in the two-step heat treatment is to promote a decrease in grain boundary resistance with the treatment in N_2 at intermediate temperature and to promote the oxidation of the surface that will be exposed to the electrolyte at a low temperature. Heat treatment at low temperatures is fundamental to avoid the diffusion of O_2 through the grain boundary.

Fig. 6 shows the current potential curves of sintered electrodes with heat treatment in different atmospheres under front-side illumination. As a general trend, the hematite photoanode under illumination shows a very poor photoelectrochemical activity. Only the sintered electrode with two-step treatment showed a significant photo-response, with an onset around 1.0 V *vs.* RHE and a photocurrent of 2.1 μA cm^{-2} (at $V_{RHE} = 1.23$) (see the inset of Fig. 6).

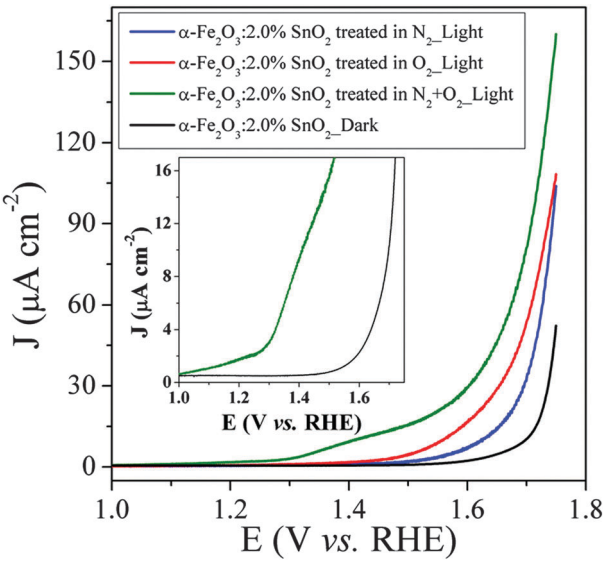

Fig. 6 The current potential (*J vs. E*) curves of the sintered electrodes with heat treatment in different atmospheres under front-side illumination and under dark conditions. The inset shows a zoom of the *J vs. E* curves, where we can observe the onset potential and the photocurrent at 1.23 V *vs.* RHE.

In order to obtain more information about the electrochemical and photoelectrochemical behavior of the sintered electrodes, we performed Mott–Schottky analysis to estimate donor density (N_d) and flat band potential (V_{fb}). In this analysis, we used ε_r (dielectric constant of α-Fe_2O_3) equal to 80. The results obtained are described in Fig. 7 and Table 2. As shown in Fig. 7, a good linear fit (with a R^2 higher than 0.98 in the bias range from 0.70 to 1.35 V *vs.* RHE) was obtained for all sintered samples heat-treated in different atmospheres. The values of N_d obtained were

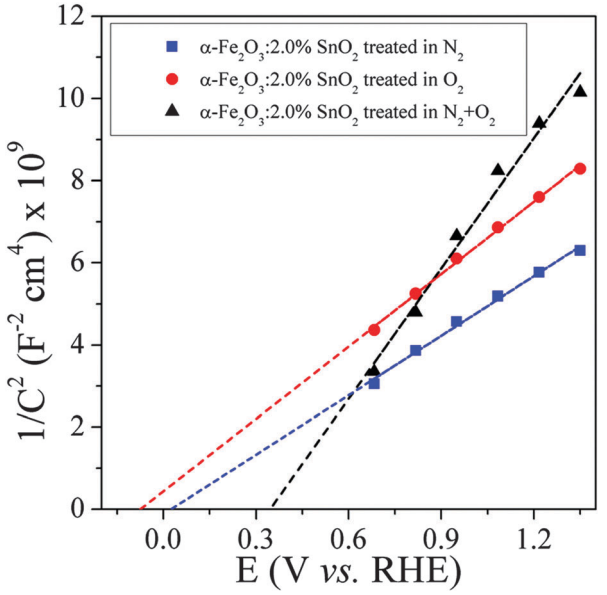

Fig. 7 Mott–Schottky plot of the sintered electrodes heat-treated in different atmospheres. These measurements were performed under dark conditions and with a frequency of 1 kHz.

Table 2 N_d and V_{fb} values measured from the Mott–Schottky analysis

Sample	V_{fb} (V *vs.* RHE)	N_d (cm^{-3})
α-Fe_2O_3:2.0% SnO_2 treated in N_2	0.03	3.7×10^{20}
α-Fe_2O_3:2.0% SnO_2 treated in O_2	−0.07	3.1×10^{20}
α-Fe_2O_3:2.0% SnO_2 treated in $N_2 + O_2$	0.34	1.7×10^{20}

in the order of 10^{20} cm^{-3}. It is interesting to note that the samples that were heat-treated in different atmospheres showed similar N_d values (see Table 2). On the other hand, V_{fb} values measured show an impressive variation and dependence on the heat treatment atmosphere. While the sample with double treatment shows a typical V_{fb} value for hematite photoanodes in the NaOH (1.0 M) electrolyte (V_{fb} = 0.34 V *vs.* RHE),[35] the samples treated in a single step show a very low V_{fb} value, *i.e.*, 0.03 V *vs.* RHE for the sample treated in N_2 and −0.07 V *vs.* RHE for the sample heat treated in O_2.

The results shown before indicate that treatment in different atmospheres modifies the electrochemical and photoelectrochemical properties of the sintered SnO_2 doped hematite photoanode. In particular, the significant modification in V_{fb} and small variation of N_d suggest a greater modification in the surface states of the electrode than in the depletion layer. We understand the term "surface state" as the electronic state induced by surface chemisorption.[36] In order to evaluate this hypothesis, we performed EIS measurements under illuminated conditions and presented the results in Fig. 8. As we can observe, the electrochemical impedance spectra (Nyquist plot) show two semicircles, one at a high frequency and another at an intermediate frequency. Based on the Bertoluzzi and Bisquert model,[7] used to analyze the kinetics of electrons and holes under photoelectrochemical water splitting conditions (under illumination), the first semicircle is related to the charge transfer in the valence band (that can be described by a *RC* parallel circuit in which *C* is the semiconductor capacitance and *R* the trapping/de-trapping resistance of the hole from the valence band) and the second one corresponds to the charge transfer in the surface state (that can be described by a *RC* parallel circuit in which *C* is the trap chemical capacitance associated with the surface state capacitance and *R* is the charge-transfer resistance). We can notice that the atmosphere affects the semicircle associated with surface state capacitance and charge-transfer resistance (the second semicircle). Assuming that the surface state dominates the charge transfer process, the sintered hematite electrode treated in the two-step procedure showed the smallest charge-transfer resistance. This result supports the previous hypothesis that the atmosphere affects the surface state and that carrying out the treatment in an oxygen atmosphere improves the charge transfer process, decreasing the charge-transfer resistance. It is important to point out that the treatment in N_2, which decreased the grain boundary resistance (solid–solid interface), is not the suitable atmosphere to promote a better charge transfer to the electrolyte.

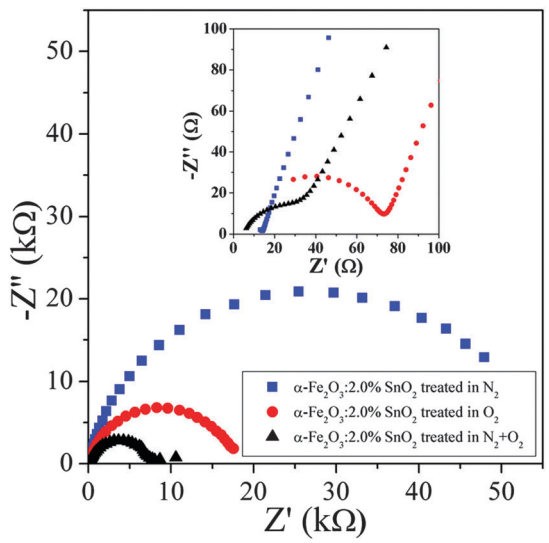

Fig. 8 EIS measurement (Nyquist plot) performed under illumination (at 1.34 V *vs.* RHE) for the samples heat-treated in different atmospheres. The inset shows the details of the first semicircle in high frequency.

Conclusions

Here, we have shown (using TEM and impedance spectroscopy) that a donor dopant such as Sn^{4+} incorporates in a heterogeneous way in the hematite. Our results show that during the sintering process, the Sn segregates to the grain boundary, decreasing its resistance and consequently, increasing the hematite conductivity. It is clear that the dopant is not acting in a classical way, increasing the donor density concentration. The information reported here is fundamental to improve the performance of hematite photoanodes to promote water splitting. We can use the segregation of dopants as an important tool to modify the conductivity of photoanodes and to modify the defects that give rise to the surface states. The segregation is even more important in nanostructured photoanodes due to the high numbers of solid–solid and solid–liquid interfaces present in this class of material. The results reported here allowed us to obtain very important information about the influence of Sn^{4+} and heat treatment atmospheres on the electrical, electrochemical and photoelectrochemical behavior of sintered hematite electrodes. The main conclusions obtained at the end of this study are:

(a) The high resistance of the undoped hematite electrode is related to the presence of a negative charge (mainly O_2^-) at the grain boundary that leads to the formation of back-to-back Schottky barriers;

(b) The addition of SnO_2 decreases the resistivity of the sintered hematite electrode. HRTEM-STEM/EDS, SSIS and *J vs. E* measurements indicate that the heterogeneous incorporation of Sn^{4+} decreases grain boundary resistance. Two different hypotheses based on defect chemistry analysis were proposed to explain the experimental observation;

(c) The heat treatment in a N_2 atmosphere also contributes to the decrease of grain boundary resistance, supporting the evidence that the presence of oxygen is fundamental for the formation of a voltage barrier at the grain boundary. The N_2 atmosphere had an influence on the doped and undoped sintered electrode;

(d) The hematite sintered electrode heat-treated in different atmospheres shows different electrochemical and photoelectrochemical behavior. We observed that the heat treatment modifies the surface states of the solid–liquid interface, modifying the charge-transfer resistance. A two-step treatment, where the second treatment was performed at a low temperature and in an O_2 atmosphere, resulted in a better solid–liquid interface;

(e) Finally, we discovered that the best heat treatment atmosphere to decrease grain boundary resistance (solid–solid interface) is not the best heat treatment atmosphere to decrease charge-transfer resistance (solid–liquid interface) and a two-step treatment is proposed to suppress this obstacle.

Acknowledgements

The financial support from FAPESP (projects CEPID – 2013/07296-2), FINEP, CNPq, and CAPES (all Brazilian agencies) is gratefully acknowledged.

Notes and references

1 M. G. Walter, E. L. Warren, J. R. McKone, S. W. Boettcher, Q. Mi, E. A. Santori and N. S. Lewis, *Chem. Rev.*, 2010, **110**, 6446.
2 K. Sivula, F. Le Formal and M. Grätzel, *ChemSusChem*, 2011, **4**, 432.
3 I. S. Cho, H. S. Han, M. Logar, J. Park and X. Zheng, *Adv. Energy Mater.*, 2016, **6**, 1501840.
4 S. R. Pendlebury, A. J. Cowan, M. Barroso, K. Sivula, J. Ye, M. Grätzel, D. R. Klug, J. Tang and J. R. Durrant, *Energy Environ. Sci.*, 2012, **5**, 6304.
5 S. C. Warren, K. Voïtchovsky, H. Dotan, C. M. Leroy, M. Cornuz, F. Stellacci, C. Hébert, A. Rothschild and M. Grätzel, *Nat. Mater.*, 2013, **12**, 842.
6 L. Steier, I. Herraiz-Cardona, S. Gimenez, F. Fabregat-Santiago, J. Bisquert, S. D. Tilley and M. Grätzel, *Adv. Funct. Mater.*, 2014, **24**, 7681.
7 L. Bertoluzzi and J. Bisquert, *J. Phys. Chem. Lett.*, 2012, **3**, 2517.
8 M. Barroso, C. A. Mesa, S. R. Pendlebury, A. J. Cowan, T. Hisatomi, K. Sivula, M. Grätzel, D. R. Klug and J. R. Durrant, *Proc. Natl. Acad. Sci. U. S. A.*, 2012, **109**, 15640.
9 K. M. H. Young, B. M. Klahr, O. Zandi and T. W. Hamann, *Catal. Sci. Technol.*, 2013, **3**, 1660.
10 M. R. Nellist, F. A. L. Laskowski, F. Lin, T. J. Mills and S. W. Boettcher, *Acc. Chem. Res.*, 2016, **49**, 733.
11 A. G. Tamirat, J. Rick, A. A. Dubale, W.-N. Su and B.-J. Hwang, *Nanoscale Horiz.*, 2016, **1**, 243.
12 P. S. Shinde, A. Annamalai, J. H. Kim, S. H. Choi, J. S. Lee and J. S. Jang, *Sol. Energy Mater. Sol. Cells*, 2015, **141**, 71.
13 P. S. Shinde, S. H. Choi, Y. Kim, J. Ryu and J. S. Jang, *Phys. Chem. Chem. Phys.*, 2016, **18**, 2495.
14 R. H. Gonalves and E. R. Leite, *J. Mater. Res.*, 2014, **1**, 47.
15 F. L. Souza, K. L. Lopes, E. Longo and E. R. Leite, *Phys. Chem. Chem. Phys.*, 2009, **11**, 1215.
16 H. L. Tuller and K.-K. Baek, in *Grain Boundary and Interfacial Phenomena in Electronic Ceramics*, ed. L. M. Levinson and S. Hirano, The American Ceramic Society, Ohio, 1994, pp. 19–34.
17 A. C. Larson and R. B. Von Dreele, General Structure Analysis System (GSAS), *Los Alamos National Laboratory Report, LAUR* 86-748, 1994.
18 P. Thompson, D. E. Cox and J. B. Hastings, *J. Appl. Crystallogr.*, 1987, **20**, 79.
19 E. R. Leite, A. P. Maciel, I. T. Weber, P. N. Lisboa-Filho, E. Longo, C. O. Paiva-Santos, A. V. C. Andrade, C. A. Pakoscimas, Y. Maniette and W. H. Schreiner, *Adv. Mater.*, 2002, **14**, 905.
20 R. H. Gonalves and E. R. Leite, *Energy Environ. Sci.*, 2014, **7**, 2250.
21 L. Xi, S. Y. Chiam, W. F. Mak, P. D. Tran, J. Barber, S. C. J. Loo and L. H. Wong, *Chem. Sci.*, 2013, **4**, 164.
22 R. L. Blake, R. E. Hessevick, T. Zoltai and L. W. Finger, *Am. Mineral.*, 1966, **51**, 123.
23 R. Dieckmann, *Philos. Mag. A*, 1993, **68**, 725.
24 J. Engel and H. L. Tuller, *Phys. Chem. Chem. Phys.*, 2014, **16**, 11374.
25 Y.-M. Chiang, D. Dimie III and W. D. Kingery, *Physical Ceramics Principle for Ceramic Science and Engineering*, John Wiley, New York, 1997.
26 C. Richard, A. Catlow, J. Corish, J. Hennessy and W. C. Mackrodt, *J. Am. Ceram. Soc.*, 1988, **71**, 42.
27 O. Warschkow, D. E. Ellis, J. Hwang, N. Mansourian-Hadavi and T. O. Mason, *J. Am. Ceram. Soc.*, 2002, **85**, 213.
28 K. L. Kliewer and J. S. Koehler, *Phys. Rev.*, 1965, **140**, 1226.
29 A. J. Bosman and H. J. van Daal, *Adv. Phys.*, 1970, **19**, 1.
30 M. P. Dare-Edwards, J. B. Goodenough, A. Hamnett and P. R. Trevellick, *J. Chem. Soc., Faraday Trans. 1*, 1983, **79**, 2027.
31 J. Fleig and J. Maier, *J. Eur. Ceram. Soc.*, 1999, **19**, 693.
32 J. Fleig, *Solid State Ionics*, 2000, **131**, 117.
33 A. Bandyopadhyay, J. Velev, W. H. Butler, S. K. Sarker and O. Bengone, *Phys. Rev. B: Condens. Matter Mater. Phys.*, 2004, **69**, 174429.
34 T.-Y. Yang, H.-Y. Kang, U. Sim, Y.-J. Lee, J.-H. Lee, B. Koo, K. T. Nam and Y.-C. Joo, *Phys. Chem. Chem. Phys.*, 2013, **15**, 2117.
35 A. Hankin, J. C. Alexander and G. H. Kelsall, *Phys. Chem. Chem. Phys.*, 2014, **16**, 16176.
36 W. Li, D. He, S. W. Sheehan, Y. He, J. E. Thorne, X. Yao, G. W. Brudvig and D. Wang, *Energy Environ. Sci.*, 2016, **9**, 1794.

